In-situ characterization of metal clusters supported on a birefringent substrate using reflectance difference spectroscopy

**J.M. Flores-Camacho · G. Weidlinger ·
N. Saucedo-Zeni · L.D. Sun · M. Hohage · P. Zeppenfeld**

Abstract Reflectance difference spectroscopy has been applied for the in-situ characterization of the growth of Ag cluster films on insulating birefringent $Al_2O_3(10\bar{1}0)$ substrates in the spectral range of 1.5–5 eV. Information on the individual cluster, cluster film morphology and growth are derived from the anisotropy of the in-plane plasmon resonances in comparison with scanning electron microscopy images. In particular, the evolution of the dipolar resonance has been attributed to two distinct stages of coarsening involving particle aggregation and ripening, and to the development of anisotropic particle shapes for higher Ag coverages. The effect of the formation of anisotropic electrostatic images in the birefringent substrate is used to explain the spectra even in the absence of structural anisotropies.

1 Introduction

Nanometer sized metal clusters are attracting scientific interest due to their possible technological applications in ultra-high data storage, catalysis, solar cells, and bio-sensors. The analysis of their optical response, resulting from the excitation of collective electron motion, i.e., particle–plasmon resonances, provides an important access to the underlying physical properties [1–3]. Optical methods such as extinction/absorption, spectroscopic ellipsometry (SE), and surface difference reflectivity (SDR) allow the post-growth analysis of the sample morphology [4, 5], from the formation of very small isolated particles [6] through the detection of collective effects among particles [7] and the percolation threshold [8] at higher coverage, to the completion of a continuous layer [9]. In addition, real-time spectroscopic ellipsometry (RTSE) has been used, e.g., to determine the average radius of embedded spherical clusters in real time in a non-invasive way [10].

The systems presented in this work consist of Ag clusters (average radii between 1 and 10 nm) forming a two-dimensional layer supported on a birefringent insulating substrate. In the following we will also refer to these clusters as particles, in the sense that they are "*particles composed of a certain number N of atoms*" [2] ($3 \leq N \lesssim 10^7$). Within the classification of *cluster-matter* by Kreibig and Vollmer [2], the present cluster layers can be considered, in most cases, as composed of separated single particles, whose joint optical response can be modeled by the mean field theory, lattice gas model [11], or renormalized polarizability approximation [12]. In the latter two cases, randomness can be included and the calculated line shapes become more similar to those obtained experimentally. However, during some stages of growth aggregates of close (but individual) particles may form [7] giving rise to strong lateral variations of the local filling fraction. Likewise, ripening of some particles through mass transfer from smaller clusters to larger ones or upon cluster coalescence may take place, which leads to the for-

J.M. Flores-Camacho · G. Weidlinger · N. Saucedo-Zeni ·
L.D. Sun · M. Hohage · P. Zeppenfeld (✉)
Institut für Experimentalphysik, Johannes Kepler Universität
Linz, Altenbergerstr. 69, 4040 Linz, Austria
e-mail: peter.zeppenfeld@jku.at

J.M. Flores-Camacho
e-mail: flores@fhi-berlin.mpg.de

G. Weidlinger
e-mail: guenther.weidlinger@jku.at

N. Saucedo-Zeni
e-mail: nadia.zeni@gilupi.de

L.D. Sun
e-mail: lidong.sun@jku.at

M. Hohage
e-mail: michael.hohage@jku.at

mation of larger particles and a concomitant decrease of the particle density.

In this work, we present an in-situ characterization during the growth of Ag clusters on laterally anisotropic $Al_2O_3(10\bar{1}0)$ substrates by means of reflectance difference spectroscopy (RDS), also termed reflection (or reflectance) anisotropy spectroscopy (RAS). A complete description of the RDS technique and its technical implementation can be found in [13–16]. RDS measures the difference in reflectivity at normal incidence for two orthogonal, linear polarizations of the incident light, which are aligned with the in-plane optical eigenaxes of the sample. This is commonly expressed as

$$\frac{\Delta r}{r} = 2\frac{r_x - r_y}{r_x + r_y}, \tag{1}$$

where r_i ($i = x, y$) are the complex reflection coefficients of the medium for the i-polarization of the incoming light. The switching between these two orthogonal linear polarization states is achieved by a combination of a Rochon linear polarizer and a photo-elastic modulator; the light reflected from the sample passes through an analyzer, and is then spectrally separated by a monochromator (spanning a photon energy range from 1.5 to 5.5 eV), and collected by a photomultiplier tube [15]. Due to the normal incidence of light, in the case of two-dimensional cluster layers, RDS is sensitive to the anisotropy of the in-plane (1, 1) plasmon modes, only. The reflectance-difference (RD) signal contains contributions related to (1) a *screening* effect, which describes the absorption of the layer grown on an anisotropic substrate [17, 18], and (2) one or more *intrinsic* effects, which correspond to the lifting of the degeneracy of the in-plane modes caused by the ellipsoidal shape of the particle [19–21], the anisotropic interaction between particles arranged in a low symmetric array [22–25], or by anisotropic images forming in the birefringent substrate [17]. The screening contribution is proportional to the planar component of the surface susceptibility γ, whereas the intrinsic effects give rise to a differential-like line shape $\propto d\gamma/dE$. RDS has been successfully applied for the characterization and in-situ monitoring during growth of semiconductor surfaces [26] and, more recently for the study of metal surfaces [27], organic molecules on substrates [18, 28] and biaxially extruded polymers [29]. Its capability to filter out the isotropic bulk response also makes of RDS a suitable tool for the study of buried interfaces and low-dimensional systems if they show some form of lateral anisotropy. In contrast to other very sensitive techniques such as SDR, RDS is instrumentally reference-free, which avoids dealing with source drifting. Furthermore, the acquisition of normalized differences in form of AC signals greatly reduces errors and noise, and thus allows measurements of opti-

cal anisotropies of the order of only 10^{-4}, depending on the particular instrument and the reflectivity of the samples.

In a preceding work, Witkowski et al. [19], have used RDS to investigate self-ordered one or two monolayer high Co islands on a gold vicinal surface. In their modeling of the RD spectra the authors could safely neglect the contribution of the Au substrate to the polarizability of the Co islands, due to the flat, disc-like shape of those particles [30]. In the present case, however, Ag tends to form spheroidal particles on the anisotropic oxide surface and we must consider the role of the substrate birefringence in the interpretation of our experimental results.

2 Experimental description

The Ag clusters were prepared in a UHV chamber (base pressure $p \leq 5 \times 10^{-10}$ mbar) by depositing Ag onto $Al_2O_3(10\bar{1}0)$ substrates at room temperature by means of a UHV-evaporation source (EFM3i, Omicron/Focus) operated in ion suppression mode. A controlled Ag deposition rate of 0.1 nm/min was used. Two methods of growth with similar results were employed, an interrupted mode used to measure spectral scans at a given nominal film thickness, during which the Ag flux remained blocked, and a continuous mode to study the real-time behavior of selected features at a fixed photon energy during Ag deposition. The commercial RD spectrometer (Horiba Jobin Yvon) was attached to the growth chamber in front of a low-strain optical viewport.

The Epi-ready, orientation marked $Al_2O_3(10\bar{1}0)$ substrates were supplied by SurfaceNet. Atomic force microscopy analysis showed flat surfaces with mean square roughness of 4 Å. No additional cleaning was performed. The optical properties and anisotropy of the bare substrate were determined before Ag deposition by ex-situ SE and in-situ RDS, respectively, resulting in a Cauchy-like line shape $n_c^s = \sqrt{\varepsilon_c^s} = A + BE^2 + CE^4$ for the c-axis, where $A = 1.759$, $B = 3.2 \times 10^{-3}$ eV^{-2}, $C = 3 \times 10^{-5}$ eV^{-4}, and the superscript s stands for substrate; the measurement of the extinction coefficient yielded a value of zero over the whole spectral range for both crystalline directions, indicating that the surfaces are mostly clean and well defined, however some carbon contamination and small amorphization of the first layers cannot be discarded. A constant anisotropy of $\Delta\varepsilon^s \approx 0.03$ was measured over the spectral range of interest (1.5–5 eV) with both SE and azimuth-dependent RDS [31].

After Ag growth, some samples were taken to a scanning electron microscope (SEM) for further analysis. The SEM measurements were performed immediately after extraction from the UHV chamber to minimize tarnishing effects. The

images were acquired by means of a Leo Supra 35 scanning electron microscope. In order to minimize charging of the insulating substrate an acceleration voltage of 4 kV was applied. The In-Lens detector was used.

3 Results and discussion

We present in Fig. 1(a) a series of RD spectra recorded after different stages of growth up to a nominal film thickness $d = 3.8$ nm. With increasing Ag coverage the spectra develop a variety of features detaching negatively from the substrate background birefringence. Due to the RDS geometry, all these features are related to the in-plane $(1, 1)$ particle–plasmon modes. The spectra are composed of resonances of dipolar character, which dominate in the first stages of growth and shift to lower energy with increasing film thickness [4], and quadrupolar resonances (Q_1, Q_2) [32] appearing at the later stages of growth. In Fig. 1(b) we show the differences between consecutive spectra of Fig. 1(a) normalized to the thickness increment. This plot emphasizes the gradual changes occurring during growth. In particular, it reveals the evolution of the dipolar resonance, which changes faster than the quadrupolar ones and thus appears more pronounced in the incremental spectra. Details of the line shapes will be discussed further below.

Selected spectral features can also be monitored at fixed photon energies as a function of deposition time, or nominal film thickness d, as shown in Fig. 2. In the following we will refer to this type of scans as "RD transients". For instance, setting the RD instrument at 3.62 eV one can follow the onset and evolution of the dipolar resonance at the
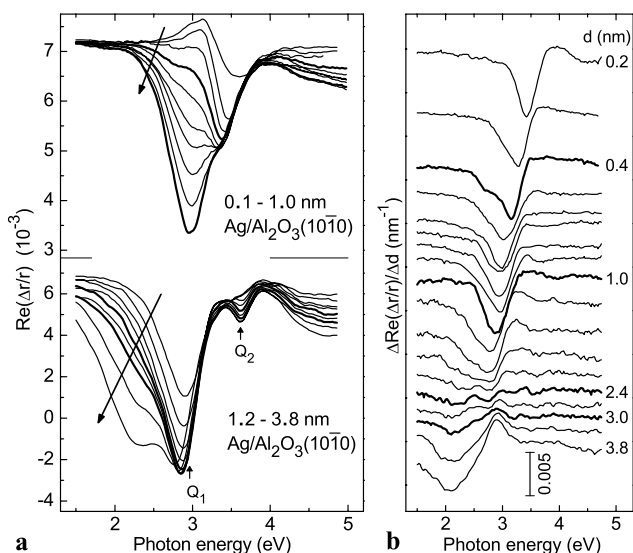
earliest stages of growth, as well as the subsequent formation of the Q_2 resonance identified in Fig. 1 and centered at this energy in the thickness range of 1.2 to at least 3.8 nm. We are thus using a quadrupolar resonance (or the energy where it eventually appears) to monitor the growth of the cluster layer in real time. Interrupted-mode readouts at other selected energies are also plotted for comparison.

Combining the information of the RD spectra and the RD transients in Figs. 1 and 2, respectively, we find that (1) the dipolar resonance undergoes a significant redshift which is associated with an increase of the cluster oblateness [4, 5, 33], truncation [34], and/or increasing particle interaction by homogeneously incrementing the two-dimensional filling fraction [3, 11, 12, 35]. (2) This dipolar resonance starts to develop a shoulder at the low energy side which becomes most pronounced at a nominal thickness around 0.4 nm, as highlighted in Figs. 1(a) and (b). As discussed later, this splitting is an indication of the presence of particle aggregates. In the same thickness range the RD transient in Fig. 2 for 3.62 eV exhibits a local maximum. For $d > 1.2$ nm, the quadrupolar resonances start to develop, giving rise to another bump in the RD transient for 3.62 eV. (3) For the highest Ag coverages the incremental contribution to the dipolar resonance peak acquires a differential line shape after passing through a stage (for $2.4 \le d \le 3$ nm) where the incremental RD spectra in Fig. 1(b) vanish almost completely. This effect is also responsible for the minimum around $d \sim 2.6$ nm in the RD transient for 2.86 eV.
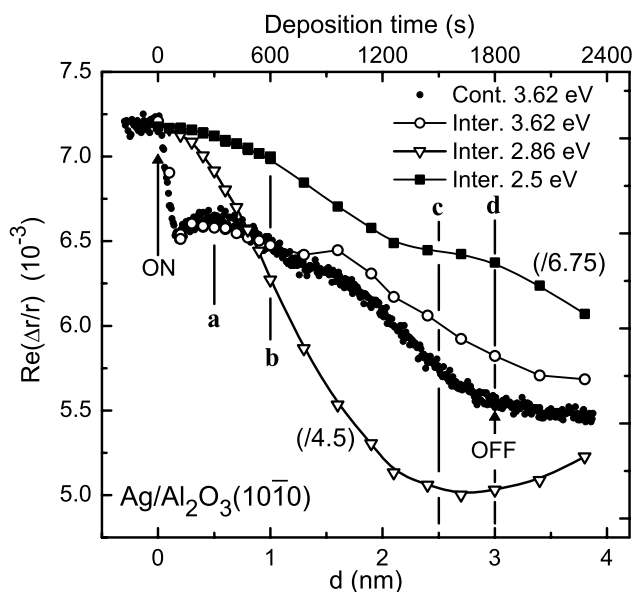

Fig. 1 (**a**) RD spectra for Ag/Al$_2$O$_3$(10$\bar{1}$0). The spectra were separated in two plots for clarity. The *arrows* indicate increasing nominal film thickness. (**b**) Subtraction of consecutive RD spectra normalized to the thickness increment

Fig. 2 Amplitude of the RD signal at selected energies for continuous (*small dots*) and interrupted growth modes (*large symbols*) as a function of deposition time and nominal film thickness d. The labels (**a**)–(**d**) in Fig. 2 refer to the corresponding SEM images in Fig. 3. The curves corresponding to readouts at photon energies of 2.86 and 2.5 eV were scaled (factors indicated) for comparison with the smaller feature at 3.62 eV
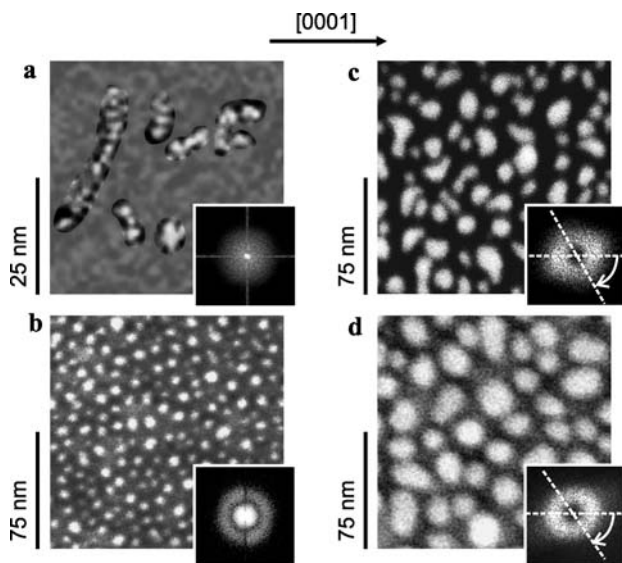
Fig. 3 SEM images of $Ag/Al_2O_3(10\bar{1}0)$ for a nominal Ag film thickness of (**a**) 0.5 nm, (**b**) 1.0 nm, (**c**) 2.5 nm, and (**d**) 3.0 nm. In (**a**) the contrast in some regions was locally enhanced for better illustration of the cluster morphology. The direction of the *c*-axis is indicated at the *top* of the figure (*arrow* along [0001]). The *insets* show the corresponding FFT power spectra. For the structurally anisotropic shapes in (**c**) and (**d**) the orientation of the major axis of anisotropy (in real space) is indicated as the *dashed line* departing from the horizontal

In order to relate the above observations to the actual morphology of the cluster layer, we have recorded SEM images for those thicknesses d at which the major optical changes occur (vertical lines in Fig. 2). The SEM images for $d = 1.0$ and 3.0 nm (Figs. 3(b) and (d), respectively) show well separated individual particles with relatively simple and compact shapes. On the other hand, the images for $d = 0.5$ and 2.5 nm (Figs. 3(a) and (c), respectively) are mostly composed of particles with irregular shapes or particles arranged into larger aggregates. Some examples of chains of two or more particles, 2D aggregates, and isolated particles are highlighted in Fig. 3(a). We also find that the average structural anisotropy of the clusters, which was estimated from the ellipticity of the two-dimensional power spectra (see insets in Figs. 3(a)–(d)), is negligible for the lower film thicknesses ($d = 0.5$ and 1.0 nm) but increases for $d = 2.5$ and 3.0 nm. Imaging small Ag thicknesses turns out to be difficult since, on one hand, the reactivity of the Ag clusters to ambient air increases with decreasing particle size, and on the other hand, the small amounts of metal on the oxide surface increment the charging of the insulating substrate even at low acceleration voltages. The former is more critical as it may possibly alter the cluster layer morphology.

The SEM images provide important clues for the interpretation of the RD results: The shape and arrangement of the particles in Figs. 3(a) and (c) suggest two stages of coarsening of the particles, one after the deposition of ~ 0.4 nm

Ag, the other as a result of particle coalescence at a later stage. The characteristic changes in the curvature of the RD transients in Fig. 2 for thicknesses around 0.4 nm and 2.5 nm can thus be related to these two coarsening stages, respectively. At the same time, the profile of the dominant dipolar contribution to the RD spectra, changes its shape, as revealed in Figs. 1(a) and (b): In the thickness range $0.3 \leq d \leq 0.7$ nm the dipolar resonance exhibits a shoulder at low energies which we attribute, in accordance with the SEM image of Fig. 3(a), to particle aggregation which induces a splitting of the in-plane resonance into a transverse and longitudinal mode for particles arranged in pairs or longer chains [36]. Likewise, Taleb et al. showed experimental evidence of asymmetric spectra or even clear shoulders forming at the low energy side of the in-plane resonance of randomly distributed particles, and correlated their findings to the presence of already coalesced and almost touching particles aggregated in chains [37].

Our hypothesis is further supported by model simulations of the RD response associated with the longitudinal and transverse plasmon modes for linear aggregates (chains) of three identical particles (top panel of Fig. 4(a)). The splitting between the longitudinal and transversal modes is maximized, independently of the particle size, for a chain of ~ 10 particles [36]. Here we have chosen a chain of only three particles mainly for illustration purposes, but also because in the present disordered system longer chains are only rarely observed (see Fig. 3(a)). Based on the SEM image in Fig. 3(a) and our previous analysis in [17], we assume oblate and truncated particles with $R_\parallel = 2$ nm, $R_\perp = 1.85$ nm, truncation parameter $t = D/R_\perp = 0.6$ and a center to center distance between neighboring particles of 4.1 nm ($>2R_\parallel$). Here $R_\parallel$ and $R_\perp$ denote the in-plane and out-of-plane radii of the particle, respectively, and $D = 1.11$ nm is the distance from the center of the figure to the substrate. The calculations are based on the quasi-static dipolar interaction model for very close particles [38, 39]. For this calculation, we have used a Drude line shape for the bulk silver free-electron region of the spectrum (which reproduces the experimentally measured Ag dielectric function for photon energies below ~ 4 eV). The electrostatic images were introduced as a second triplet just below the dividing interface (the substrate surface). The associated image dipole moments depend on the cluster geometry and on the dielectric properties of the substrate, namely its dielectric function and birefringence [17, 40]. To make our calculation consistent with the observed structural isotropy of the film at the initial stages of growth, i.e., with the fact that the chain axes are stochastically oriented, we have treated the case of chains oriented along either of the two optical eigenaxes of the birefringent substrate. In the absence of structural anisotropy a non-vanishing RD signal is then obtained only if the screening effect and the anisotropic images forming in the birefringent
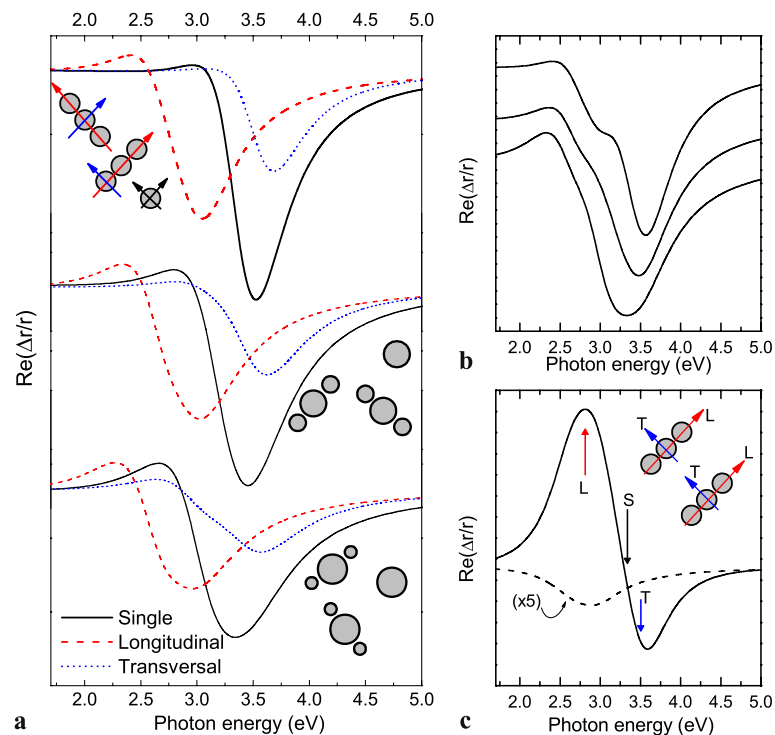
Fig. 4 (**a**) Resonances of longitudinal (*dashed line*) and transversal (*dotted line*) chain modes for truncated oblate Ag particles with a radius of 2 nm separated by 4.1 nm. The *solid lines* show the calculated line shape for a single particle. *Top panel*: Response of two orthogonally oriented triplets of identical particles. *Center* and *bottom panels*: Changes in the line shapes in response to a mass transfer from the outer two particles to the central particle. Schematics of the particle configurations are shown next to the corresponding spectra. (**b**) Corresponding sums of the three contributions for each stage presented in (**a**). (**c**) Resulting spectrum for aligned chains (*solid line*). The screening part of the signal is plotted separately for illustration: Its amplitude is similar to the longitudinal modes presented in (**a**)

substrate are taken into account in the calculation [17]. The final RD spectrum contains contributions from the longitudinal and transverse chain modes as well as from the single degenerate mode of individual (non-interacting) particles. These three contributions are obtained from the anisotropic aggregate response

$$\Delta\eta_m = \eta_m^c - \eta_m^a, \tag{2}$$

where η is the effective polarizability of the aggregates with the index m denoting the longitudinal, transversal, or non-interacting mode (single particle), respectively and c, a are the eigenaxes of the substrate. Equation (2) implies that the RD spectrometer was aligned in such a way that a maximum positive signal was measured on the bare substrate before Ag deposition. It should be clarified that by adding the net anisotropic response of a particular aggregate and individual particles, we are simulating the contributions of the characteristic building blocks of the cluster layer and not that of the whole heterogeneous sample.

The results are shown in the top panel of Fig. 4(a). For illustration, the result of the individual particle was scaled by a factor of 2. A clear splitting of the modes for the chain configuration is obtained, which depends on the inter-particle

distance: the closer the particles are in the chain, the larger the redshift of the longitudinal mode with respect to the single particle resonance [41]. Together, the three contributions give a line shape with a shoulder at the low energy side which is quite similar to the experimental RD spectrum in Figs. 1(a) and (b) for a nominal Ag thickness of 0.4 nm as seen in the top spectrum of Fig. 4(b).

Beyond a nominal film thickness $d = 0.5$ nm the modes tend to merge into a single feature at $d = 1$ nm (Fig. 1(b)). Based on the discrete dipole approximation, it has been demonstrated in [38] that this can be explained by particle sintering via the formation of a common grain boundary. We performed further simulations to evaluate the effect of ripening, i.e., one particle gaining mass over its neighbors (keeping, for simplicity, the total volume and cross section area of the triplet constant). The center to center distance between clusters was set to $R_{||,side} + R_{||,center} + 0.1$ nm. The spectra at the center and bottom of Fig. 4(a) show that in this case the splitting is being reduced (basically because the particle in the center is getting slightly flatter, thus its resonance is redshifted), and in this way the resonances will eventually merge. This result is also in agreement with electrodynamic calculations for a pair of unequal interacting spheres [42]. The process of obtaining a single particle-like resonance at

Fig. 5 Real (**a**) and imaginary (**b**) parts of the incremental net contributions (*thick red lines*) when the film thickness is increased from 2.4 to 2.7 nm (*top*) and from 3.4 to 3.8 nm (*bottom*). The parameters used in the calculation are listed in Table 1. In the *lower panel*, the total difference spectrum is separated into its three constituents (*thin blue lines*): the incremental anisotropic shape contribution (*solid line*), the incremental anisotropic image contribution (*dashed line*), and the contribution of the incremental screening effect (*dotted line*). The *open circles* are the corresponding experimental curves of Fig. 1(b)
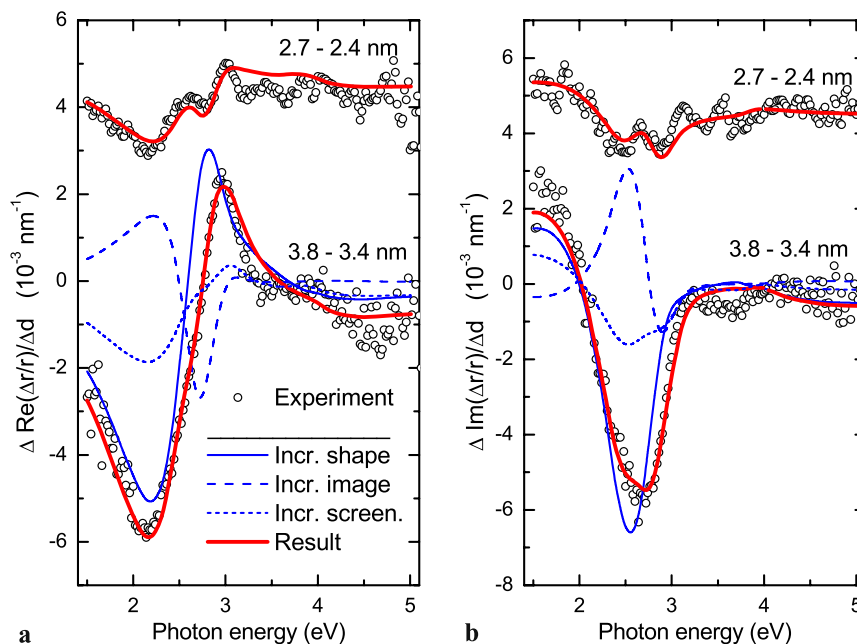
a nominal film thickness of 1 nm is then explained by the combined contribution of particle sintering and the transfer of mass to one particle from its neighbors (ripening). The sum of the three modes is presented in Fig. 4(b). The diminishing influence of the longitudinal mode and the broadening of the total spectrum represent quite well the situation of the experimental spectra between $d = 0.4$ nm and $d = 1$ nm in Fig. 1(b). It is noted that, if the chains were aligned, the RD spectrum would have a differential-like line shape and its amplitude would be much larger than in the disordered system. This is shown in Fig. 4(c), where a calculation of the anisotropy of longitudinal (L) and transversal (T) modes in an ensemble of non cross-talking chains is compared to the screening contribution of the same system. The latter (scaled by a factor of 5 for clarity) is of comparable amplitude as the curves in Fig. 4(a). It is very likely, given the line shape and the relatively high amplitude of the 0.1 nm Ag spectrum in Fig. 1(a), that at the first stages of growth some preferential ordering (e.g., at step edges) is taking place. Unfortunately, we were not able to check this with SEM since particles of very small sizes are much more reactive to ambient air.

The semi-quantitative simulation of spectra corresponding to the non-aggregated morphology depicted in Figs. 3(b) and (d) for $d = 1$ and 3 nm have already been presented elsewhere [17], but part of those results will be used in the following.

Upon particle coalescence and ripening at $d \sim 2.5$ nm the particles acquire a more ellipsoidal shape, reducing the in-plane structural symmetry. This shape contribution to the intrinsic optical anisotropy may eventually outweigh the anisotropic image effect. As a result, the line profile of the incremental RD spectra will change from a negative peak

Table 1 Parameters used for the calculations in Fig. 5, where the Feret radius is the radius of a circle with the same area as the average actual cluster, n is the number density of particles, S_z is the shape ratio, and S_{xy} is the in-plane anisotropy

Nominal thickness	Feret radius (nm)	n (nm^{-2})	S_z	S_{xy}
1.0	3.00	0.0070	1.406	1.00
2.4	4.91	0.0028	1.476	0.90
2.7	5.50	0.0025	1.482	0.89
3.4	6.53	0.0019	1.530	0.85
3.8	7.55	0.0016	1.550	0.83

to a differential-like line shape. In fact, even the transitory quenching of the signal observed for $d \sim 2.4$ nm in Fig. 1(b) can be explained by the fortuitous cancelation of these two competing intrinsic contributions to the optical anisotropy. This is illustrated in Fig. 5 where the calculated contributions to the incremental RD signal associated with the anisotropic image effect (dashed line), the anisotropic cluster shapes (solid line) and the change of volume of the cluster layer, i.e., the incremental screening effect (dotted line) are shown separately. The calculations are based on the structural parameters deduced from the SEM images in Fig. 3, the results reported in [17], and the dielectric function of Ag tabulated in the literature [43]. All parameters are listed in Table 1. According to the FFT power spectra (insets in Figs. 3(c) and (d)), we have assumed an ensemble of particles which, on average, have a slightly elliptical shape with the major axis oriented at 55±5° with respect to the principal optical axis (*c*-axis) of the substrate. This orientation, within experimental errors, has been recently observed for

larger Au clusters on the clean $Al_2O_3(10\bar{1}0)$ substrate [44]. Due to this azimuthal offset, the shape-related contribution to the optical anisotropy will have the opposite sign as compared to the image effect (see lower panel in Fig. 5). Taking into account the average structural anisotropy as determined from Fig. 3(c), an almost complete cancelation of the two contributions is obtained for $2.4 \le d \le 3$ nm, resulting in a transitory quenching of the incremental RD signal as observed in Fig. 1(b). Besides the morphological information provided by SEM, we have used spectroscopic ellipsometry to correctly place the present in-plane resonances in relation to the out-of-plane particle mode [17], since the center of the resonance is also influenced by the height of the particles. We note that the contribution of the anisotropic clusters to the RD spectrum should be much larger (more than one order of magnitude) than the anisotropic image effect, if the major axis of the elongated clusters were perfectly aligned. Due to the considerable amount of disorder in the present system, this is not the case and the calculated curves in Fig. 5 illustrating the effect of anisotropic shapes were thus scaled by an arbitrary factor, which, however, was held constant for all the considered film thicknesses.

The real and imaginary parts of the resulting curves should be compared to the experimental spectra of Fig. 1(b) for the corresponding thickness. We find that, by slightly adapting the in-plane aspect ratio S_{xy}, the calculated line shapes are in excellent agreement with the experiment. In [17] we used $S_{xy} = 0.87$ for the tarnished 3.8 nm Ag layer, whereas the simulation of in-situ spectra required slightly different S_{xy} values as indicated in Table 1. In Table 1, we also present for each nominal film thickness the Feret radius $R_\parallel$ (which is defined as the radius of a circular particle with the same in-plane area as the actual average cluster), the number density of particles n, and the shape ratio $S_z = (2R_\parallel/R_\perp)/(1+t)$. For particles with radii between 2 and 10 nm the size does not determine the energy of resonance (which justifies a quasi-static approximation). However, both the out-of-plane geometry as defined by S_z and n are critical for the placement of the center of resonance. These parameters are average values, which however, represent quite well the actual morphology of the sample as demonstrated below with the aid of Fig. 6. Note that the average S_{xy} in Table 1 follows a systematic *elongation* trend as a function of incrementing coverage. It is also noted that, as shown in Fig. 5(d) of [17], this trend is also related to the particle size: larger particles tend to be more elliptical when growing on the anisotropic oxide substrate. Due to tarnishing, which is a phenomenon affecting rapidly the particles exposed to ambient air, not only the quadrupolar resonances are lost [32], but also the average S_{xy} is slightly modified.

The FFT power spectra in the insets of Fig. 3(c) and (d) reveal that, although there is a hint for a preferential orientation of the average ellipsoidal particle, the distribution of both aspect ratios S_{xy} and angular orientations of the major axes is quite broad. A more realistic simulation would require considering, besides the parameters discussed above, the interaction among particles of different sizes, aspect ratios and angular orientations in the plane of the substrate. Such a simulation requires a lot of individual particles, and thus it is not very practical for gaining further physical information for the required computational costs. Analysis of individual contributions, on the other hand, is simpler and very illustrative. As an example we show in Fig. 6 the effect of a broad angular distribution of the major axes of the elongated particles. For this we have fixed the dimensions and in-plane aspect ratio $S_{xy} = 0.9$ for all particles. The particles are arranged in a hexagonal array with all major axes lying in the plane of the hexagon. Furthermore, as we are only interested in inter-particle interactions, the substrate was removed (free floating particles) and, thereby, the electrostatic images. Also, for simplicity we used only the Drude contribution to the Ag bulk dielectric function. The polarizability tensor was rotated individually for each particle in the array and then the dipolar interaction [38, 39] between particles of different orientations was obtained in the quasi-static approximation. The modified polarizability of the particle in the center due to different orientations of the major axes of its neighbors was used then as the input for the calculation of the RD spectra. The result is shown in Fig. 6. The schematic arrays indicate the cases of (1) all particles equally oriented at 120° with respect to the x-axis, (2) all the neighbors oriented at 90° with respect to the particle in the center, and (3) an intermediate case, in which the neighbors are oriented at different angles (in units of 30° with respect to x). From
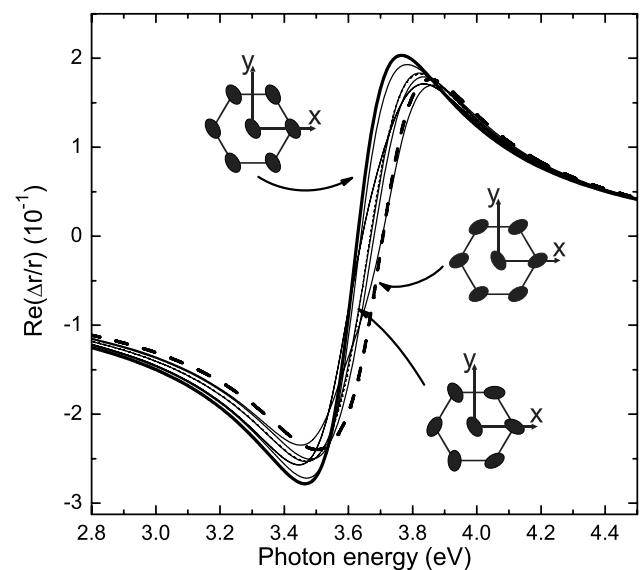

Fig. 6 Calculated RD spectra for a particle in the center of a free-floating hexagonal ensemble of ellipsoidal particles for different orientations of the major axes of its neighbors (the orientation of the particle in the center was kept fixed)

this simulation we conclude that the distribution width in the orientation of the major axes around a certain average angle leads to an inaccuracy in the determination of the energy of the center of resonance of the curves presented in Fig. 5 of $\Delta E = \pm 38$ meV which translates into an error of at most 3% in the estimation of the height of the particles, which is the parameter that places the resonance if the lateral dimensions of the cluster are known. The error in S_{xy} is of the order of 2%. This was estimated by fitting values of S_{xy} for different heights of the average cluster. Therefore, deviations from the simulated S_{xy} with respect to those measured from the SEM images are explained not only by changes of morphology due to exposition to ambient air, as discussed above, but also by the shielding of the dipolar interaction between clusters due to the formation of a dielectric shell around the particles.

As illustrated in the bottom panels of Fig. 5, the anisotropic shape contribution has the same sign as the incremental screening effect. Therefore, the quenching of the incremental RD signal at $d \sim 2.5$ nm (top panels of Fig. 5) can only be explained by the competition with a third source of anisotropy, namely the anisotropic image contribution, with opposite sign. This confirms our previous assumption of the non-negligible influence of the anisotropic images on the RD spectra.

4 Conclusions

Reflectance difference spectroscopy was used to study the evolution of the anisotropic optical response as a function of nominal film thickness for a system of Ag particles deposited on the birefringent $Al_2O_3(10\bar{1}0)$ substrate. Spectra can be recorded in-situ during growth and have been analyzed in terms of dipolar and quadrupolar particle resonances. The effects of filling fraction, coarsening in the form of particle aggregation and ripening, as well as the development of shape anisotropy during the later stages of growth have been identified. In addition, the presence of the anisotropic electrostatic images forming in the birefringent substrate leads to a non-vanishing RD spectrum even in the absence of structural forms of anisotropy.

References

1. S. Norrman, T. Andersson, C.G. Granqvist, O. Hunderi, Phys. Rev. B **18**, 674 (1978)
2. U. Kreibig, M. Vollmer, *Optical Properties of Metal Clusters*. Springer Series in Materials Science, vol. 25 (Springer, Berlin, 1995)
3. D. Bedeaux, J. Vlieger, *Optical Properties of Surfaces* (Imperial College Press, London, 2002)
4. T. Wenzel, J. Bosbach, F. Stietz, F. Träger, Surf. Sci. **432**, 257 (1999)
5. R. Lazzari, I. Simonsen, D. Bedeaux, J. Vlieger, J. Jupille, Eur. Phys. J. B **24**, 267 (2001)
6. Y. Borensztein, P. De-Andrès, R. Monreal, T. Lopez-Rios, F. Flores, Phys. Rev. B **33**, 2828 (1986)
7. D. Schönauer, M. Quinten, U. Kreibig, Z. Phys. D **12**, 527 (1989)
8. A.J. de Vries, E.S. Kooij, H. Wormeester, A.A. Mewe, B. Poelsema, J. Appl. Phys. **101**, 053703 (2007)
9. B. Dusemund, A. Hoffmann, T. Salzmann, U. Kreibig, G. Schmid, Z. Phys. D **20**, 305 (1991)
10. T.W.H. Oates, Appl. Phys. Lett. **88**, 213115 (2006)
11. B.N.J. Persson, A. Liebsch, Phys. Rev. B **28**, 4247 (1983)
12. R.G. Barrera, M. del Castillo-Mussot, G. Monsivais, P. Villaseñor, W.L. Mochán, Phys. Rev. B **43**, 13819 (1991)
13. D.E. Aspnes, J.P. Harbison, A.A. Studna, L.T. Florez, J. Vac. Sci. Technol. A **6**, 1327 (1988)
14. L.F. Lastras-Martínez, A. Lastras-Martínez, R.E. Balderas-Navarro, Rev. Sci. Instrum. **64**, 2147 (1993)
15. O. Acher, B. Drévillon, Rev. Sci. Instrum. **63**, 5332 (1992)
16. P. Weightman, D.S. Martin, R.J. Cole, T. Farrell, Rep. Prog. Phys. **68**, 1251 (2005)
17. J.M. Flores-Camacho, L.D. Sun, N. Saucedo-Zeni, G. Weidlinger, M. Hohage, P. Zeppenfeld, Phys. Rev. B **78**, 075416 (2008)
18. C. Goletti, G. Bussetti, R.E. Chiaradia, A. Sassella, A. Borghesi, Appl. Phys. Lett. **83**, 4146 (2003)
19. N. Witkowski, Y. Borensztein, G. Baudot, V. Repain, Y. Girard, S. Rousset, Phys. Rev. B **70**, 085408 (2004)
20. N. Esser, A.M. Frisch, A. Röseler, S. Schintke, C. Goletti, B.O. Fimland, Phys. Rev. B **67**, 125306 (2003)
21. S. Chandola, J. Jacob, K. Fleischer, P. Vogt, W. Richter, J.F. McGilp, J. Phys., Condens. Matter **18**, 6979 (2006)
22. S. Linden, J. Kuhl, H. Giessen, Phys. Rev. Lett. **86**, 4688 (2001)
23. E. Fort, C. Ricolleau, J. Sau-Pueyo, Nano Lett. **3**, 65 (2003)
24. W. Rechberger, A. Hohenau, A. Leitner, J.R. Krenn, B. Lamprecht, F.R. Aussenegg, Opt. Commun. **220**, 137 (2003)
25. S. Camelio, D. Babonneau, D. Lantiat, L. Simonot, Europhys. Lett. **79**, 47002 (2007)
26. I. Kamiya, D.E. Aspnes, L.T. Florez, J.P. Harbison, Phys. Rev. B **46**, 15894 (1992)
27. D.S. Martin, N.P. Blanchard, P. Weightman, D.S. Roseburgh, R.J. Cole, J.-K. Hansen, J. Bremer, O. Hunderi, Phys. Rev. B **76**, 115403 (2007)
28. L.D. Sun, M. Hohage, P. Zeppenfeld, S. Berkebile, G. Koller, F.P. Netzer, M.G. Ramsey, Appl. Phys. Lett. **88**, 121913 (2006)
29. K. Schmidegg, L.D. Sun, P. Zeppenfeld, Appl. Phys. Lett. **89**, 051906 (2006)
30. P.A. Bobbert, J. Vlieger, Physica A **147**, 115 (1987)
31. B.F. Macdonald, J.S. Law, R.J. Cole, J. Appl. Phys. **93**, 3320 (2003)
32. R. Lazzari, S. Roux, I. Simonsen, J. Jupille, D. Bedeaux, J. Vlieger, Phys. Rev. B **65**, 235424 (2002)
33. T. Yamaguchi, S. Yoshida, A. Kinbara, Thin Solid Films **21**, 173 (1974)
34. M. Wind, J. Vlieger, D. Bedeaux, Physica A **141**, 33 (1987)
35. T. Yamaguchi, S. Yoshida, A. Kinbara, Thin Solid Films **18**, 63 (1973)

36. M. Quinten, U. Kreibig, Appl. Opt. **32**, 6173 (1993)
37. A. Taleb, V. Russier, A. Courty, M.P. Pileni, Phys. Rev. B **59**, 13350 (1999)
38. T. Jensen, L. Kelly, A. Lazarides, G.C. Schatz, J. Cluster Sci. **10**, 295 (1999)
39. L. Gunnarsson, T. Rindzevicius, J. Prikulis, B. Kasemo, M. Käll, S. Zou, G.C. Schatz, J. Phys. Chem. B **109**, 1079 (2005)
40. S.C. Schneider, S. Grafström, L.M. Eng, Phys. Rev. B **71**, 115418 (2005)
41. J.M. Gérardy, M. Ausloos, Phys. Rev. B **25**, 4204 (1982)
42. J.M. Gérardy, M. Ausloos, Phys. Rev. B **27**, 6446 (1983)
43. P.B. Johnson, R.W. Christy, Phys. Rev. B **6**, 4370 (1972)
44. H. Sadan, W.D. Kaplan, J. Mater. Sci. **41**, 5371 (2006)